Center for Synchrotron Biosciences' U2B beamline: an international resource for biological infrared spectroscopy

N. S. Marinkovic,[a,b] R. Huang,[a,b] P. Bromberg,[a,b] M. Sullivan,[a,b] J. Toomey,[a,b] L. M. Miller,[c] E. Sperber,[d] S. Moshe,[d] K. W. Jones,[e] E. Chouparova,[e] S. Lappi,[f] S. Franzen[f] and M. R. Chance[a,b]*

[a]Center for Synchrotron Biosciences, Albert Einstein College of Medicine, 1300 Morris Park Avenue, Bronx, NY 10461, USA, [b]Department of Physiology and Biophysics, Albert Einstein College of Medicine, 1300 Morris Park Avenue, Bronx, NY 10461, USA, [c]National Synchrotron Light Source, Brookhaven National Laboratory, Upton, NY 11973, USA, [d]Department of Neuroscience, Albert Einstein College of Medicine, 1300 Morris Park Avenue, Bronx, NY 10461, USA, [e]Department of Applied Science, Brookhaven National Laboratory, Upton, NY 11973, USA, and [f]Department of Chemistry, North Carolina State University, Raleigh, NC 27695, USA.
E-mail: mrc@aecom.yu.edu

A synchrotron infrared (IR) beamline, U2B, dedicated to the biomedical and biological sciences has been constructed and is in operation at the National Synchrotron Light Source (NSLS) of Brookhaven National Laboratory. The facility is operated by the Center for Synchrotron Biosciences of the Albert Einstein College of Medicine in cooperation with the NSLS. Owing to the broadband nature of the synchrotron beam with brightness 1000 times that of conventional sources, Fourier transform IR spectroscopy experiments are feasible on diffraction-limited sample areas at high signal-to-noise ratios and with relatively short data-acquisition times. A number of synchrotron IR microscopy experiments that have been performed in the mid-IR spectral range (500–5000 cm^{-1}) are summarized, including time-resolved protein-folding studies in the microsecond time regime, IR imaging of neurons, bone and other biological tissues, as well as imaging of samples of interest in the chemical and environmental sciences. Owing to the high flux output of this beamline in the far-IR region (50–500 cm^{-1}), investigations of hydrogen bonding and dynamic molecular motions of biomolecules have been carried out from 10 to 300 K using a custom-made cryostat and an evacuated box. This facility is intended as an international resource for biological IR spectroscopy fully available to outside users based on competitive proposal.

Keywords: infrared spectroscopy; microscopy; biological imaging; bone; protein folding; nucleic acid dynamics.

1. Introduction

It is widely known that infrared (IR) spectroscopy has the ability to identify molecular constituents from their vibrational spectra. This so-called molecular fingerprint is found in the part of the IR spectrum often called the mid-IR region, and has been investigated in research laboratories and in industry for decades. In biological samples, primary components include lipids, proteins, nucleic acids and carbohydrates, all of which have unique spectral features in the mid-IR region. The dominant absorption features in the lipid spectrum are found in the region 2800–3000 cm^{-1}, and are assigned to antisymmetric and symmetric stretching vibrations of CH_3 (2956 and 2874 cm^{-1}) and CH_2 (2922 and 2852 cm^{-1}) groups of the acyl chains. In addition, the strong band at 1736 cm^{-1} arises from ester $C{=}O$ groups in the lipid. The protein spectrum has two primary features, the amide I (1600–1700 cm^{-1}) and amide II (1500–1560 cm^{-1}) bands, which arise from specific stretching and bending vibrations of the peptide backbone. The frequency of the amide I band is particularly sensitive to protein secondary structure. The nucleic acid spectrum also displays $C{=}O$ stretching vibrations from the purine (1717 cm^{-1}) and pyrimidine (1666 cm^{-1}) bases. In addition, the region between 1000 and 1500 cm^{-1} contains contributions from antisymmetric (1224 cm^{-1}) and symmetric (1087 cm^{-1}) PO_2^- stretching vibrations (Miller *et al.*, 2000).

Over the past 20 years, biological samples have been examined with IR microscopes in order to spatially resolve inhomogeneous samples and small particles. While this IR microspectroscopic technique offers good spectral quality when relatively large areas (*i.e.* several tens of micrometers) are investigated, the throughput from the conventional thermal (globar) source is insufficient in applications that require a spatial resolution at the diffraction limit (Carr, 2001). This has limited the investigation of biological specimens to the tissue level. Furthermore, the globar source is also inadequate in performing far-IR spectroscopy experiments that examine biological dynamics and metal–ligand vibrational modes (Xie *et al.*, 1999). The globar source has its peak flux (*i.e.* number of photons produced per unit time) in the mid-IR region, and the output drops by four orders of magnitude when the wavelength changes from 1 to 1000 µm (Williams, 1990).

Synchrotron IR sources are ideal for overcoming these specific difficulties. The primary advantage of synchrotron IR light is its brightness (defined as the photon flux or power emitted per source area and solid angle), which is 100–1000 times greater from a synchrotron source (Duncan & Williams, 1983). This brightness advantage is not because the synchrotron produces more power, but because the effective source size is small and the light is emitted into a narrow range of angles. High brightness is desirable for any measurement with a limited 'throughput', meaning either a small sample area, the requirement of a narrow beam, or a combination of both. Microspectroscopy is perhaps the best-known example of a measurement with low throughput, and the synchrotron source is well suited to this technique.

A laser IR source is also bright and can supply a high photon flux onto a small aperture. However, unlike a laser, the synchrotron source is broadband in nature so that spectroscopy and curve-fit analyses can be performed easily. Furthermore, since the photon flux of the synchrotron source decays only to about half when the wavelength changes from 1 to 1000 µm, the use of the new light source proves to be very effective in the far-IR region. Although the use of synchrotron radiation as a source in IR spectroscopy emerged recently, it has rapidly become an important application of new storage-ring technology. Research using IR radiation from synchrotron sources has seen a steady growth over the last ten years (Williams, 1990; Melendres, 1998). Today, more than half of some 40 operating storage-ring synchrotron radiation sources around the globe have at least one IR beamline either in operation or under construction (see, for instance, http://www-ssrl.slac.stanford.edu/sr_sources.html, http://www-elsa.physik.uni-bonn.de/accelerator_list.html). Facilities for IR synchrotron radiation can be found throughout the world, serving to produce light for the scientific community. The National Synchrotron Light Source (NSLS, Brookhaven National Laboratory) presently operates six IR beamlines, making it a premier synchrotron facility for IR investigations (Carr *et al.*, 1998). Active IR beamlines can also be found at UVSOR, Okasaki (Japan); ALS, Berkeley and SRC, Stoughton (USA). In Europe, IR activities continue at the SRS, Daresbury (UK); LURE, Orsay (France); MAXLAB, Lund (Sweden); and at Daφne, Frascati (Italy). Other facilities that are either planning or considering IR programs include Diamond, Rutherford Laboratory (UK); ESRF, Grenoble and Soleil, Paris (France); BESSY II, Berlin, ANKA, Karlsruhe and DELTA, Dortmund (Germany); Duke-FEL, Durham (USA); CLS, Saskatoon (Canada); LNLS, Campinas, (Brazil); CAMD, Baton Rouge, (USA); SURF-3, Gaithersburg (USA); NSRL, Hefei (China); SPring-8, Nishi-Harima (Japan); and SRRC, Hsinchu (Taiwan). While IR microscopy is a very common application associated with synchrotron IR research, other active programs, such as vacuum and high-pressure surface science, electrochemistry and biology, are progressing rapidly.

The Albert Einstein Center for Synchrotron Biosciences' U2B beamline is located on the VUV-IR ring of the National Synchrotron Light Source. The U2 extraction port chamber was installed in the VUV ring in December 1996. The mirror box that divides the light for the use of two equal end stations (U2A and U2B) was installed in October 1997, and the remainder of the beamline in March 1998. After conditioning, it took full beam on 15 May 1998. U2A and U2B end-stations were then constructed, and each took light in November 1998. The U2B beamline has been in full operation and has been accepting outside users since the spring of 2000, after a commissioning period of one year. Although dedicated primarily to bioscience measurements, its users also perform measurements in environmental sciences, as well as in applied physics and chemistry. In this publication we report on its present capabilities, available instrumentation and give several examples of the current research performed at U2B to demonstrate that this beamline is a valuable resource and is ready to serve the international scientific communities.

2. Beamline description, instrumentation and capabilities

U2 is a synchrotron IR port delivering ~80 mrad horizontally by 40 mrad vertically. The synchrotron beam is steered and focused by a combination of ellipsoidal and planar mirrors to provide a 1:1 image of the source. The beam passes through a series of valves and masks (see Fig. 1), then through a wedged diamond window into a mirror box where it is divided into two equal lines (U2A and U2B). The beam that is steered toward U2B beamline continues through a rough vacuum-pumped tube and then through a window (KBr or polyethylene, depending on the desired frequency range) into the nitrogen-purged instrumentation listed below. The total angular acceptance is 45 H × 40 V mrad.

The beamline is equipped with a dry nitrogen-purged Fourier transform infrared (FTIR) spectrometer (Magna 860, Thermo Nicolet Instruments, Madison, WI, USA), a Nicolet NicPlan IR microscope, and a custom-made external cryostat chamber. The spectrometer is equipped with a Michelson interferometer having capabilities such as rapid scan, step-scan and the ability to accept external beams and utilize external detectors. For measurements in its internal chamber, a narrow-band mercury–cadmium telluride (MCT/A) and a deuterated triglycine sulfate (DTGS) detector with polyethylene window are available, covering a range from 5000 to 100 cm^{-1}. A number of transmission cells for liquid samples are also available (Sealed Precision Pathlength Cell, Thermo Spectra-Tech, Shelton, CT, USA). The sample temperature can be regulated by a heated/cooled cell holder (Model HC-32 Demountable Cell Kit, Thermo Spectra-Tech) using a re-circulating bath.

The doubly confocal NicPlan IR microscope is outfitted with a full range of objectives, such as 10× and 20× visible objectives, a 32× IR objective (Thermo Spectra-Tech) for both transmission and reflection IR measurements, and an attenuated total reflection (ATR) ZnSe objective (Thermo Spectra-Tech) for reflection measurements of highly absorbing and/or thick samples. The microscope is capable of diffraction-limited spatial resolution. It is equipped with a computer-controlled stage that brings the sample under the objective. Fully automated IR microscopic experiments can be performed using *Atlμs* software (Thermo Nicolet) with the possibility to view the visual image of the sample together with its three-dimensional IR representation (IR map). For measurements in transmission mode, a full range of IR-transparent windows (BaF$_2$, CaF$_2$, ZnSe *etc.*) as support for mounting samples, and a diamond anvil cell (Thermo Spectra-Tech) are available. IR-reflective microscope slides (Low-e Microscope Slides, Kevley Technologies, Chesterland, OH, USA) and custom-made gold-coated microscope slides can be used for mounting samples for measurements in reflection mode.

In order to broaden the range of vibrational spectra collected by the microscope, a flat pick-off mirror has been introduced in the optical path to allow the use of external detectors. The mirror directs the light either to the internal narrow-band MCT/A detector operating in the 7000–650 cm^{-1} range, or to the external detectors. With the use of external detectors, the lower frequency limit of the spectra obtained through the microscope is extended, at the expense of the

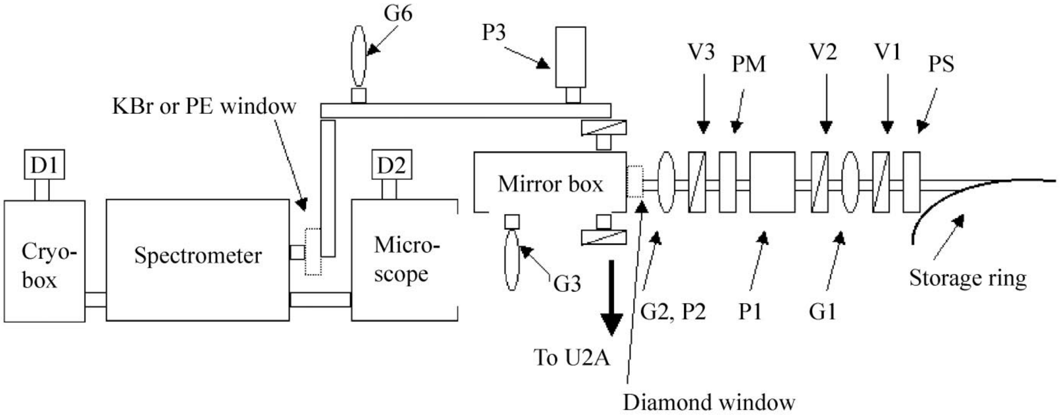

Figure 1
Schematic presentation of the U2B beamline layout. P1, P2: high-vacuum pumps; P3: rough pump; V1, V2 *etc*: valves; G1, G2 *etc*: vacuum gauges; PS: photon shutter; PM: photon mask; D1, D2: external detectors.

signal-to-noise ratio. Three detectors are placed behind the microscope: a liquid-nitrogen-cooled broadband MCT/B detector (Belov Technology, New Brunswick, NJ, USA) operating in a 5000–450 cm^{-1} spectral range with a sensor size of 0.25 × 0.25 mm, a liquid-helium-cooled dual-detector system (Infrared Laboratories, Tucson, AZ, USA) combining a silicon bolometer with a wedged white polyethylene window that covers the far-spectral range (650–10 cm^{-1}), and an Si:B photodetector with a KRS-5 window for measurements in the mid-IR (3500–350 cm^{-1}). The signal-to-noise ratio is the highest for MCT/A (3–8 times higher than MCT/B, depending on the frequency, while that of the Si:B photodetector is comparable with MCT/B around 600 cm^{-1}, yet improved twofold around 450 cm^{-1}). With the use of the bolometer, the lower frequency limit can be extended to about 30 cm^{-1}. A set of motorized and manual translation stages and collimating optics are placed behind the microscope to precisely align the external detectors. The complete optical path, from the spectrometer through the microscope and to the detectors, is continuously purged with dry nitrogen to insure a significant reduction in water vapor absorption that would otherwise render portions of both the mid-IR and far-IR unusable.

The U2B beamline is further equipped with a custom-made external chamber that can be either purged or evacuated. Its 6″ focal-length focusing mirror illuminates a sample of about 2 mm in diameter and directs the partially absorbed light from the sample to a detector. The chamber is equipped with a cold finger (Janis ST-100) that cools the sample temperature to 4.2 K (liquid-helium temperature). Powder, liquid or crystal samples up to 7 mm in diameter can be placed in the holder. Combined with a temperature controller and computer control (Lake Shore, model 330), a continuous set of spectra as a function of temperature can be automatically collected in both the mid- and far-IR by means of the wide-range MCT/B detector with sensor size 1 × 1 mm, and the liquid-helium-cooled dual-detector system described above, respectively.

3. Microsecond to millisecond IR spectroscopy

The brightness of a synchrotron source results in spectra with good signal-to-noise ratios for a small sampling area with a relatively short data-collection time. This advantage may be exploited in the study of the submillisecond protein folding using time-resolved FTIR microscopy, where spatial and spectral resolution as well as data-collection time are important experimental constraints.

A number of optical techniques (CD, UV/fluorescence, Raman), in combination with ultrafast mixers, have been implemented to study fast protein-folding kinetics (Eaton *et al.*, 2000; Brockwell *et al.*, 2000). However, FTIR microscopy, in conjunction with our rapid-mixing continuous-flow apparatus, is also a powerful technique for examining the early stages of protein refolding. FTIR spectroscopy has been used extensively to study protein structure; the amide I band profile (1600–1700 cm^{-1}) is considered to be the most sensitive probe for monitoring changes in the secondary structure of proteins (Haris & Chapman, 1995). Development of our turbulent-mixing rapid-mixing FTIR microscopy technique has been accomplished by examining the refolding kinetics of cytochrome-*c* under various chemical conditions (Marinkovic *et al.*, 2000; Bromberg *et al.*, 2002). It should be noted that diffusional mixers have recently been used in conjunction with an FTIR microscope to examine protein folding; their performance would be enhanced using a synchrotron source (Kaufmann *et al.*, 2001).

The initial design of our rapid-mixing continuous-flow cell (Marinkovic *et al.*, 2000) has been modified and optimized to permit spectral collection in the 0.23 to 5.0 ms time window of a reaction (Fig. 2). The flow cell is composed of a ZnSe window package that contains an observation channel (52 × 200 µm) connected to a mixing groove (100 × 100 µm) *via* a thin seal (120 µm thick). The mixed solution emerges from a hole in the seal (254 µm diameter) into the observation channel; the dead time for turbulent mixing and passage of the solution through the seal, together, is *ca.* 200 µs. Using a FTIR microscope, a globar or synchrotron IR source is focused at various positions along the groove through a 100 µm or 10 µm upper aperture, respectively. The timescale of each spectrum is determined from the solution velocity in the observation channel, the distance between the focal point and the seal, and the dead time of the mixer and seal together. The timescale error of the experiment is determined from the size of the upper aperture. The first observation point of high signal-to-noise quality lies at 300 µm from the seal. Thus, at our highest reasonable flow rate (3.0 ml min^{-1}), 230 µs is the lowest timescale accessible with the current flow cell. Good quality spectra can be obtained using 128 or 64 scans at 4 cm^{-1} resolution, and about 10 ml of 0.5 or 1 m*M* protein solution is required to achieve informative kinetic data with several data points.

Time-resolved FTIR microscopy has been used to evaluate the refolding kinetics of acid-denatured cytochrome-*c* to a molten globule and the native state, induced by exposure to high salt and pH-jumps, respectively (Bromberg *et al.*, 2002). The kinetic analyses involved measuring the time-dependence of the amide I component bands assigned to solvent-exposed coil (1669 cm^{-1}), buried α-helices (1655 cm^{-1}), unordered structure (1645 cm^{-1}), and solvated α-helices (1633 cm^{-1}). The rates of helix formation were comparable with rates obtained by other optical techniques using similar turbulent mixing devices and chemical conditions, illustrating the utility of rapid-mixing time-resolved FTIR microscopy as a complementary tool for

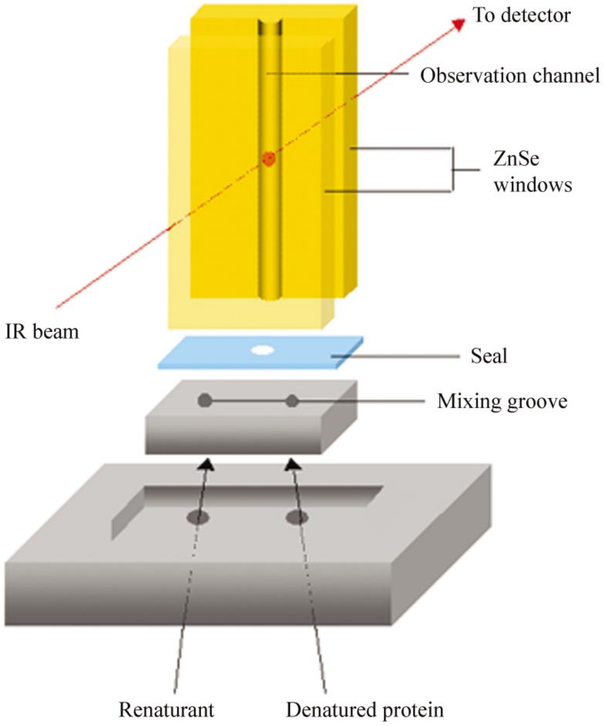

Figure 2
Schematic of the rapid-mixer flow cell for time-resolved measurements by IR spectroscopy. Denatured protein and renaturant separately enter the mixing groove (100 µm wide, 100 µm deep) and the resultant solution flows into the observation channel (200 µm wide, 52 µm deep) bored in one of the two ZnSe windows, through a 254 µm-wide hole in a 120 µm-thick seal.

examining submillisecond events in protein refolding. However, unlike other optical techniques, FTIR is also suitable for examining more complex biological mixtures. Therefore, rapid-mixing time-resolved FTIR microscopy could be potentially useful in discerning the kinetics and mechanisms of a wide assortment of bimolecular reactions relevant to biology (*i.e.* enzyme–substrate binding kinetics, protein–lipid interactions, protein–nucleic acid interactions *etc.*) provided that the kinetic rate constants of the reactions are within 5000 and 200 s^{-1}. Moreover, if the window package is constructed from quartz, the cell design may be suitable for use with other spectroscopies (for instance, synchrotron CD) for studying conformational changes of proteins, carbohydrates and nucleic acids.

4. IR mapping of cells and tissues

Although conventional IR microspectroscopy has proven extremely valuable for resolving the chemical components in biological samples, existing instruments using a conventional IR source encounter a signal-to-noise limitation when apertures confine the IR to an area of 20–30 μm in diameter. This constrains the analysis of biological specimens to the tissue level only. Individual biological cells are typically 5–30 μm in diameter, making them too small to probe with a conventional IR source. The high brightness of the synchrotron source allows smaller regions to be probed with acceptable signal-to-noise (Reffner *et al.*, 1995; Carr *et al.*, 1995). Indeed, aperture settings smaller than the wavelength of light can be used, though, in this case, diffraction controls the available spatial resolution (Carr & Williams, 1997). Thus, for a typical biological specimen, the diffraction-limited spatial resolution for primary lipid (C—H stretch), protein (amide I), and nucleic acid (P—O stretch) absorption features is approximately 3, 6 and 12 μm, respectively. Thus, the synchrotron source permits chemical imaging within single cells, allowing the detection of chemical variations at sub-cellular levels. Although the synchrotron source is bright, the total power delivered to a sample area of 10 × 10 μm is less than 5 mW (Martin *et al.*, 2001), which is non-destructive to living cells as demonstrated on mitotic and dying cells at another NSLS beamline (Jamin *et al.*, 1998*a*,*b*). In the following sections, two examples from recent experiments performed at U2B are presented to demonstrate that synchrotron FTIR microspectroscopy is advantageous in studying microscopic biological systems.

4.1. IR microscopy studies of epilepsy and neurodegeneration in animals

Hippocampal tissue from humans with chronic temporal lobe epilepsy reveals a specific pattern of neuronal degeneration referred to as mesial temporal sclerosis (Sloviter *et al.*, 1996; Sperk, 1994). The predominant feature of this disease includes a selective loss of pyramidal neurons in the hippocampal endblades and frequently in the Sommer sector, *i.e.* CA3 and CA1 areas, respectively. In contrast, pyramidal cells in the transitional zone between the two areas (CA2 area), as well as granular cell layer, subiculum and fibers *en passage* remain intact (Sperk, 1994; Sperk *et al.*, 1994). Kainic acid is often used to induce seizures in animals. Neuronal loss is apparent at 24 h, and is maximal at 48 h after the onset of kainic acid status epilepticus. A wide variety of morphological changes associated with dying during development or following a toxic insult are observed in cells. A binary classification scheme suggests that physiologically appropriate death is due to apoptosis and that pathological mechanisms involve necrosis (Charriaut-Marlangue *et al.*, 1996). Necrosis, or accidental or pathological cell death, is characterized by rupture of the membrane due to swelling of organelles, so that cytoplasmic contents are released into the extracellular space. In contrast, apoptosis, or physiological cell death, is characterized by nuclear condensation and cellular and membrane shrinkage. Apoptosis has been reported to increase following a wide range of pathological states, such as those induced by neurodegenerative diseases (Charriaut-Marlangue *et al.*, 1996), adrenalectomy (Sloviter *et al.*, 1996) and seizure (Piekut *et al.*, 1997).

We have used visible and IR images of a healthy and diseased neural tissue to observe changes in the pyramidal neurons in the CA3 and CA1 regions. The samples were prepared as follows. An adult rat was exposed to severe status epilepticus and sacrificed by transcardiac perfusion 48 h after the onset of seizure. The normal rat had a sham injection. The brain was fixed overnight in the same perfusate and left in 30% sucrose solution. When the brain sunk it was rapidly frozen in methylbutane (233 K) and cut through the dorsal hippocampus in a cryostat (255 K) into 12 μm-thick sections. The tissue was mounted onto BaF_2 windows and placed under the IR microscope. The IR maps of CA1, CA2 and CA3 pyramidal cells and surrounding tissue were collected using 64 scans with 4 cm^{-1} resolution. The aperture size was 10 μm, which is roughly the size of a pyramidal cell (see Fig. 3), and the stage was moved in 10 μm increments. The protein, lipid, disulfide, ketone and phosphate mid-IR regions were examined to assess biochemical differences in the tissue samples.

We found that examination of the peak intensities of the amide I band to lipid bands (1654 and 2922 cm^{-1}, respectively) provided an indicator of the disease. As seen in Fig. 3, the IR image of bands closely follows the optical image, indicating that the highest amide to lipid peak ratio is found within the CA3 cells in the normal tissue. In contrast, the IR image of the tissue sample of diseased animal shows that the amide I to lipid ratio is high not only within the cells, but spreads several tens of micrometers further away from the cell wall. It appears that diseased neural cells lose their integrity, spreading their bio-material towards the surrounding tissue. This seems to indicate that necrosis was induced in hippocampal tissue. However, in order to clearly demonstrate which process occurred in the hippocampal tissue of the rats with induced seizure, further work is planned involving phosphate and nucleic acid signatures in the far-IR region (below 650 cm^{-1}) where damage by apoptosis is known to occur.

4.2. Analysis of bone chemistry in osteoporosis

Osteoporosis, characterized by decreased bone density, altered bone architecture and increased susceptibility to fracture, is a common and costly disease afflicting millions of women (Rodan & Martin, 2000). Although the role of bone density in osteoporosis is well established, little is known about the changes in bone chemistry as disease progresses. Alterations of several chemical components of bone, including carbonate, phosphate and collagen, may affect bone strength. Furthermore, in the study of heterogeneous bone tissues, chemical variations at different locations of bone, *i.e.* cortical *versus* trabecular, may be important in determining the overall mechanical properties of bone.

The application of synchrotron IR microspectroscopy to examine changes in bone chemistry in a monkey model of osteoporosis has been previously described (Miller *et al.*, 1999). The microscopic matrix and mineral chemistry of osteopenic bone were monitored by studying the peaks of IR spectra at amide I (1700–1600 cm^{-1}), carbonate ($\nu_2CO_3^{2-}$, 825–905 cm^{-1}) and phosphate ($\nu_4PO_4^{3-}$, 500–650 cm^{-1}). It has been demonstrated that the ratios between the integrated area of phosphate (or carbonate) and amide I bands represent the amount of mineral relative to matrix in bone (Paschalis *et al.*, 1996; Camacho *et al.*, 1999). Curve-fitting the three regions yields information about the compositions of mineral and matrix components that may be altered during the disease process (Miller *et*

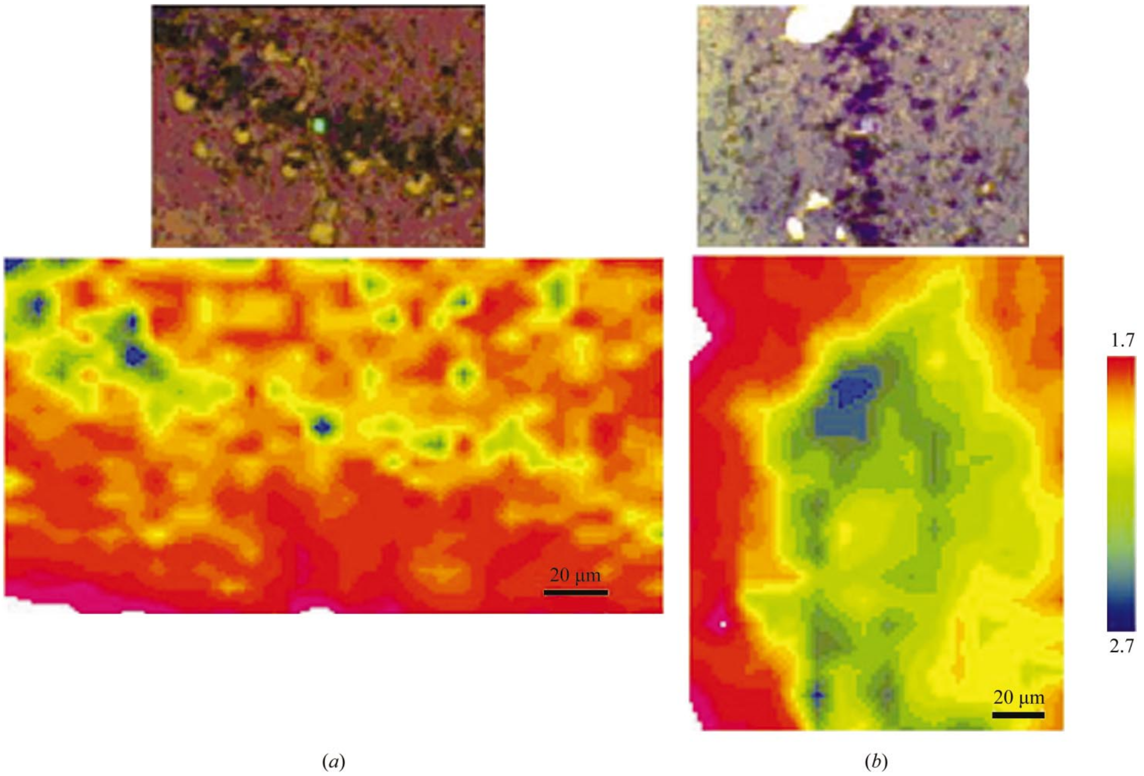

Figure 3
Optical (top) and false-colored IR images of brain tissue from (*a*) a normal rat and (*b*) a rat with severe seizure. Tissues were mounted on BaF_2 windows. The aperture size was 10 µm × 10 µm (see the green square at the center of the optical image of normal rat tissue). For each data point in the IR map, a spectrum was acquired using 64 co-additions and Happ-Genzel apodization at 4 cm^{-1} resolution. A background spectrum through a spot without sample was collected for absorbance reference. The map is generated using an amide I to lipid peak height ratio of bands at 1654 and 2922 cm^{-1}, respectively, and the color represents the intensity of the ratio.

al., 1999; Paschalis *et al.*, 1996; Camacho *et al.*, 1999; Pleshko *et al.*, 1991). To further analyze these changes, we assessed both the overall and localized bone quality using two spectral data-collection approaches: (i) mapping broad randomly selected bone regions to obtain a large number of spectra, and (ii) individual point-and-shoot at regions labeled by fluorochromes to be of a given age (Miller *et al.*, 1999) (Fig. 4). In both cases, synchrotron light source is necessary for data collection at spatial resolutions near the diffraction limit (3–20 µm) (Miller *et al.*, 2001). We studied the proximal tibiae of animals at three distinct anatomical regions: cortical, subchondral and trabecular bone. A bone-density-enhancing drug, nandrolone decanoate, was administered to a subset of ovariectomized monkeys as a comparison with the non-treated subjects to demonstrate the effect of the drug on bone chemistry during disease progression.

59 adult female cynomolgus monkeys were group-housed and fed identically for the study. The details of the trial have been described previously (Jerome *et al.*, 1997). Briefly, the subjects were assigned randomly into four treatment groups for the 24 month study: (1) Sham operated (SHAM) (*n* = 15); (2) ovariectomized, treated with placebo for two years (OVX) (*n* = 15); (3) ovx + nandrolone decanoate for two years (NAN) (*n* = 15); (4) ovx + nandrolone decanoate beginning one year after ovx (dNAN) (*n* = 14). Treated groups (NAN and dNAN) were given 25 mg nandrolone decanoate intramuscularly every three weeks and non-treated groups (SHAM and OVX) were given sterile vehicle intramuscularly every three weeks. At the time of ovariectomy (or sham operation), one year after surgery, and two weeks before

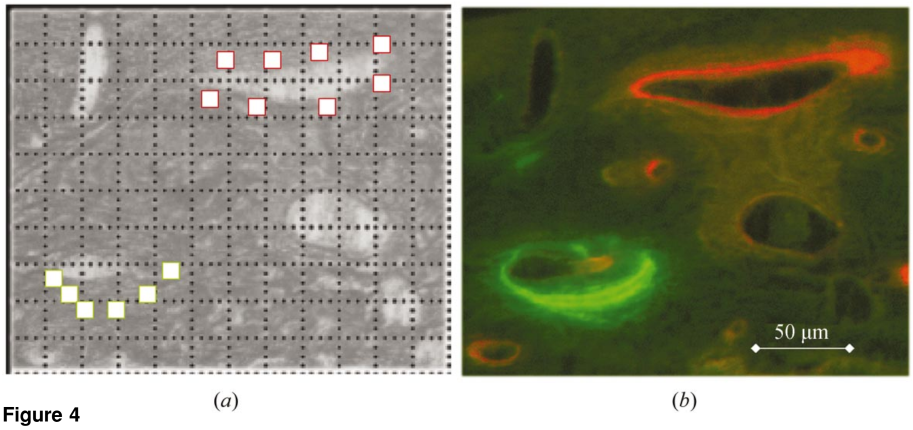

Figure 4
(*a*) 100× light image from a subchondral region of proximal tibia from one of the ovariectomized animals. The squares within the grid indicate the fields of data collection limited by a 20 µm × 20 µm aperture during mapping. White-colored squares correspond to data collection at the fluorescent labels shown in (*b*). The aperture size in this case was limited to 20 µm × 20 µm. For each data point, a spectrum was acquired using 64 co-additions and Happ-Genzel apodization at 4 cm^{-1} resolution. A background spectrum through air (no sample) was collected for absorbance reference. (*b*) Fluorescent image of the same field. Calcein (green) and alizerin complexone (red) indicate bone formed one and two years, respectively, after ovariectomy.

necropsy, all animals were administered fluorochrome labels (tetracycline HCl, calcein and alizarin complexone, respectively) intravenously on a 1-7-1-7 schedule (Jerome *et al.*, 1997). One tibia from each animal was obtained at the termination of the study. A mid-coronal section from each proximal tibia was embedded in methyl methacrylate/dibutyl phthalate. The blocks were sectioned at a thickness of 5 µm with a sledge microtome and tissue sections from five SHAM, seven OVX, six NAN and six dNAN animals were air dried and mounted in an IR sample cell.

The bone section was secured in a compression cell (Thermo Spectra-Tech) with the center portion exposed to the beam path. To study the $\nu_4PO_4^{3-}$ band (500–650 cm^{-1}), we used the external MCT/B detector (Belov Technology) that has a working range from 5000 to 450 cm^{-1}. To minimize the water vapor absorbance, the beam paths, starting from the spectrometer and ending in the external detector, were sealed and continuously purged by nitrogen gas. In the mapping mode of data collection, the IR spectra were collected into *x–y* coordinates using the *Atlµs* software (Thermo Nicolet) that controls the motorized stage. A video camera was mounted onto the microscope to capture visible-light images before each data collection. An adjustable aperture was placed in the optical path before the objective to limit the IR illumination area of each data point to 20 × 20 µm for mapping and 10 × 10 µm for point-and-shoot. The size of the aperture was calibrated using a visible-light image at its focal point. For each animal, 900, 600 and 400 spectra were collected from randomly chosen cortical, subchondral and trabecular bone regions, respectively. At all chosen regions, data acquisition was performed in a rectangular-sized map format using *Atlµs* software with 20 µm steps using the *x–y* motorized stage. A spectrum was acquired for each data point using 64 co-additions and Happ-Genzel apodization at 4 cm^{-1} resolution. Prior to starting a map, a light image of the map area was taken using the same coordinate as the map for visual guidance in later data filtering, and a background spectrum through air (no sample) was collected to convert the data to absorbance.

Prior to data processing, the maps were decomposed into separate spectral files labeled by the coordinates. A number of spectral bands for each spectrum had to be analyzed by peak fitting so that the maximum chemical information could be extracted. For the numbers of scans involved, an automated procedure to reliably analyze each spectrum was required. We developed a macro within the *Grams3.2* software (Galactic Industries Corporation, Salem, NH, USA) to automate these procedures. The initial conditions for the curve-fitting routines in the macro were determined prior to running the macro. The center positions for the sub-peaks within the three regions were determined based on previous assignments (Miller *et al.*, 2001; Rey *et al.*, 1989, 1990), and these assignments were confirmed by examining a set of collected spectra using second-derivative peak analyses. Several initial conditions were tested to ensure reproducibility and validity of the final fit for each analysis. In a macro routine, one IR absorbance spectrum was first baseline-corrected in the amide I, $\nu_2CO_3^{2-}$ and $\nu_4PO_4^{3-}$ regions (Fig. 5) using a cubic function to account for the underlying absorbance (Miller *et al.*, 2001). Curve-fitting subroutines were then utilized to analyze these three regions individually. All peaks were fitted using a sum of Gaussian functions with the center position limited to ± 2 cm^{-1} from the initial position, while the width was limited to 30 cm^{-1} (for broad bands, 40 cm^{-1} were used) to avoid alternative convergent solutions. The convergence criteria were determined by the reduced χ^2 statistics and the root-mean-square noise level. A maximum of 50 repeated optimization algorithms were carried out for each fit subroutine until the convergence criteria were met. The curve-fit subroutine then outputs the center position, width and height values, integrated area, and χ^2 value for each fitted peak. The output files generated by the *Grams3.2* macro were named according to the same *x–y* coordinates as the processed spectra. We developed a data-conversion program using Borland C++ to parse the output files from the macro to a single file in CSV format readable by Microsoft Excel. With the filter tool in Excel, we first eliminated spectra with non-convergent fits, and then

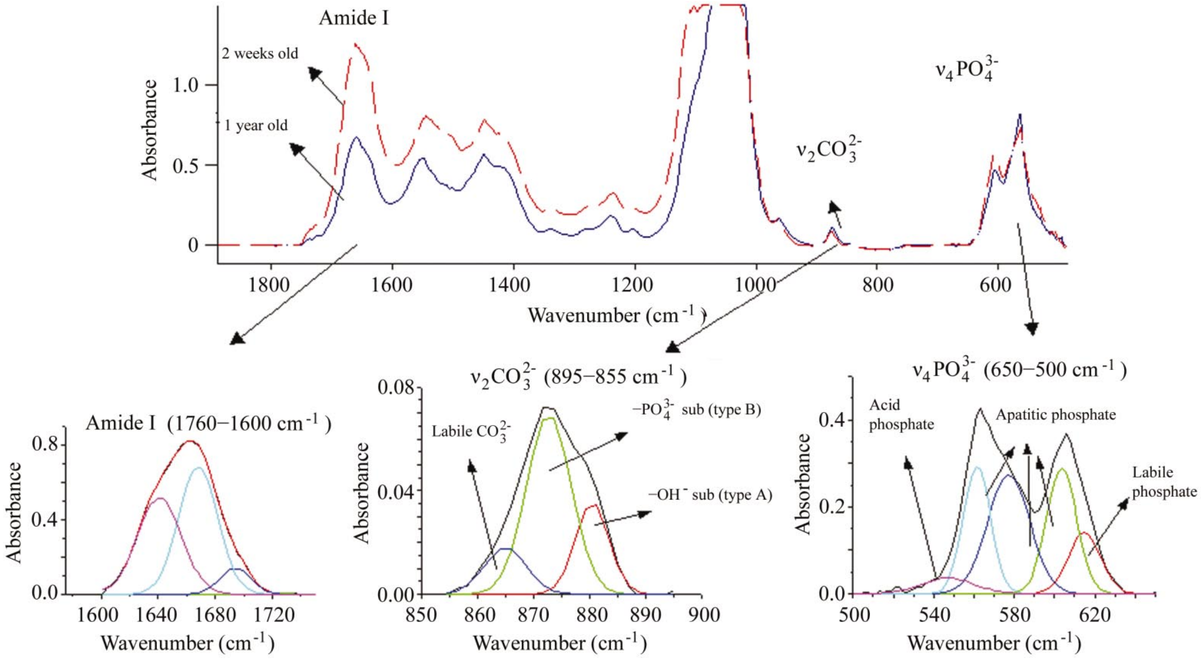

Figure 5
A baseline-corrected IR spectrum of one data-collection point. The regions analyzed by a curve-fitting method are indicated and their assignments are shown by the boxed figures below.

identified and discarded spectra from non-bone regions having higher absorption intensities between 1700 and 1760 cm^{-1} due to the presence of methyl methacrylate (embedding material). The integrated peak areas were expressed as ratios to eliminate the effects due to sample thickness heterogeneity. For each map, the calculated ratios of integrated peak areas were tabulated into histograms and fitted to normal distribution curves. Spectra collected using point-and-shoot approaches were analyzed by the same curve-fit macro routines and the resulting ratios were averaged separately for each label type in each animal.

For visual comparisons between different ratios, contour maps of ratio intensities were generated using Microcal Origin 5.0 (Northampton, MA, USA) with the same coordinate as in the data-collection field. For example, the contour map of carbonate-to-matrix ratios (Fig. 6) from the same field shown in Fig. 4 demonstrates that areas with low intensities correspond to the alizarin labeled region (red label), indicating less carbonate mineralization in the newly formed bone. By comparing the results from diseased monkeys to those from intact as well as treated subjects, we are able to detect specific changes in bone chemistry due to disease and therapy. To date, the results of macroscopic chemical changes examined by IR mapping has been reported (Huang *et al.*, 2002*a*), where a significant decrease in carbonate and increased acid phosphate content were observed in ovariectomized animals. The microscopic results combining FTIR and fluorescence microscopy further demonstrate localized changes in the amount of phosphate and carbonate as well as the degree of collagen cross-linking (Huang *et al.*, 2002*b*). These results show that synchrotron FTIR microspectroscopy can be used to study bone tissue chemistry with a level of detail that is not possible with other techniques. In particular, it has the ability to monitor both the mineral and the matrix components of bone simultaneously. In addition, the automated fitting procedures allow the chemical information of the IR spectra to be rapidly extracted such that quantitative mapping is possible.

5. Temperature-dependent far-IR study of purine nucleic acid compounds

The study of macromolecular dynamics using far-IR spectroscopy has a history of over 30 years (Itoh *et al.*, 1968; Koenig & Sutton, 1969).

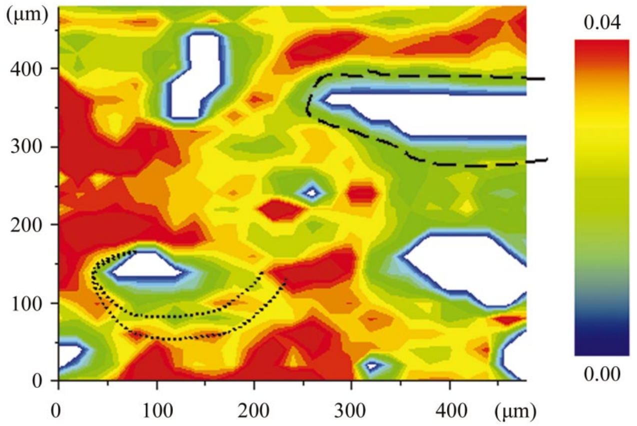

Figure 6
Contour maps of $\nu_2CO_3^{2-}$/amide I ratio from the same field shown in Fig. 4. The map was generated by tabulating the ratios obtained from curve-fitting analysis into the same *x–y* coordinate defined in Fig. 4(*a*). The intensity is represented by a color gradient indicated by the column to the right of the figure.

The advent of FTIR methods and the availability of synchrotron sources are allowing an increase in the application of far-IR spectroscopy to biological studies. Hydrogen-bonding interactions, metal–ligand interactions and collective modes of proteins, as well as large dynamical molecular motions, are generally found in the spectral region below 200 cm^{-1}. Molecular dynamic simulations show that about 15% of all vibrational modes fall into this range (Moritsugu *et al.*, 2000). Furthermore, the temperature dependence of low-frequency modes reveals their anharmonic coupling due to the change in the ground-state population relative to all excited states (Xie *et al.*, 1999, 2002). For an anharmonic transition, the energy gap between any two successive vibrational states becomes smaller as the vibrational quantum state increases, so that the frequency of the vibrational transition increases with the increase in population of the ground state. We examine the temperature dependence of the vibrational frequency to analyze the anharmonic coupling.

The IR spectrum of a compound often contains a larger number of bands that can be accounted for by normal coordinate analysis, due to combination bands, mixing and splitting of solute and solvent bands and overtones that become allowed due to anharmonicity. Stable isotopic substitution of central and peripheral atoms provides a means to alter the vibrational pattern to facilitate comparison with calculation. This method allows us to identify modes that are anharmonically coupled to low-frequency hydrogen-bonding modes. In this way, a check is obtained on the potential-energy surfaces that we calculate for the hydrogen-bonding interactions in nucleic acids.

Natural abundance adenine and 2-deoxyadenosine were purchased from Sigma Chemical Company, St Louis, MO, USA. Isotopic adenine was singly labeled with ^{13}C at positions C(2) and C(8), with ^{15}N at exocyclic amino [N(6)] and N(9), and triply labeled with ^{13}C at C(8) and ^{15}N at N(6) and N(9). Isotopic 2-deoxyadenosine was singly labeled with ^{15}N at exocyclic amino [N(6)] and N(9), doubly labeled with ^{13}C at C(8) and ^{15}N at N(9), and triply labeled with ^{13}C at C(8) and ^{15}N at N(6) and N(9). Both sets of isotopic compounds were obtained from the Stable Isotope Resource at Los Alamos National Laboratory. Deuterated derivatives of adenine and its isotopomers were prepared by way of hydrogen exchange reflux, for a minimum of 4 h, at 313 K in D_2O (Aldrich, Milwaukee, WI, USA; 99.9%). Deionized 18 MΩ water exchange was performed on all six samples of adenine as a control.

Polycrystalline samples were placed between two polyethylene windows of diameter 7 mm and thickness 0.8 mm and then mounted in the sample holder of a liquid-helium cold finger (Janis ST-100). The temperature was monitored by a Lake Shore Cryotronics temperature controller (DRC-82) using a silicon diode sensor mounted above the sample holder. The cold finger was placed into its heat shield base, which had been mounted in a vacuum box that maintained a vacuum of approximately 100 mtorr. The vacuum box was connected to the FTIR spectrometer (Thermo Nicolet) running at the mirror velocity of 633 Hz, and to the liquid-helium-cooled boron-doped silicon bolometer (Infrared Laboratories). The synchrotron radiation beam of beamline U2B was the light source for these experiments. The effective spectral window provided by this experimental setup is 40 cm^{-1} to 600 cm^{-1}.

A temperature-dependent series of far-IR absorption spectra, from 80 to 300 K, of adenine are shown in Fig. 7. The important features to note are the shifts and sharpness of the bands that occur as a result of changing temperature. Also of interest is the appearance of new bands in the 80 K spectra that are poorly resolved in the 300 K spectra. The appearance of these new bands is believed to be the result of anharmonic coupling of low-frequency modes in this polycrystalline material.

A temperature-dependent series of far-IR absorption spectra of 2-deoxyadenosine is shown in Fig. 8. Although the number of peaks for 2-deoxyadenosine is greater than that for adenine owing to the presence of ribose, the bands at 104, 139, 247, 336 and 542 cm^{-1} are the same in both compounds. Good agreement with experimental vibrational frequencies at 10 K can be obtained using density functional theory calculations. Both these calculations and extensive isotope labeling are being used to determine the strength of anharmonic coupling for the modes shown in Figs. 7 and 8.

The fact that so many low-frequency modes appear to have strong temperature dependence is somewhat surprising, given the studies of anharmonic coupling in other biological molecules (*e.g.* the axial vibrations of the heme iron in heme proteins). We plan to identify relationships that are unique to the hydrogen-bonding interaction and to obtain similar data in oligonucleotides in crystalline and glassy forms in order to determine the effect of hydrogen-bond patterns on vibrational spectra in the far-IR region (Lappi *et al.*, 2002).

6. Chemical and environmental measurements

Deposition of solid material, such as waxes and asphaltenes, in petroleum production equipment is a major problem occurring in various oil- and gas-producing regions worldwide (Lira-Galeana *et al.*, 1996; Lira-Galeana & Hammami, 2000). The solid deposits cause reduction of diameter and plugging of well equipment and pipelines, which ultimately results in an increased cost of produced oil and gas. Many questions regarding the liquid–solid phase transitions, mechanisms of nucleation, aggregation and deposition of these complex mixtures upon a change in environment are still poorly understood, which slows down the development of efficient preventive and remediation technologies.

Compositionally, the wax deposits are a complex mixture of high-molecular-weight hydrocarbons and non-hydrocarbons (resins and asphaltenes), with additional trapped oil, water and inorganic material in various proportions. As a result of changing temperature, pressure and oil composition during production, components with different chemical composition and properties can reach supersaturation at different stages and start to crystallize, aggregate and accumulate, often around nuclei such as asphaltene and fine inorganic particles.

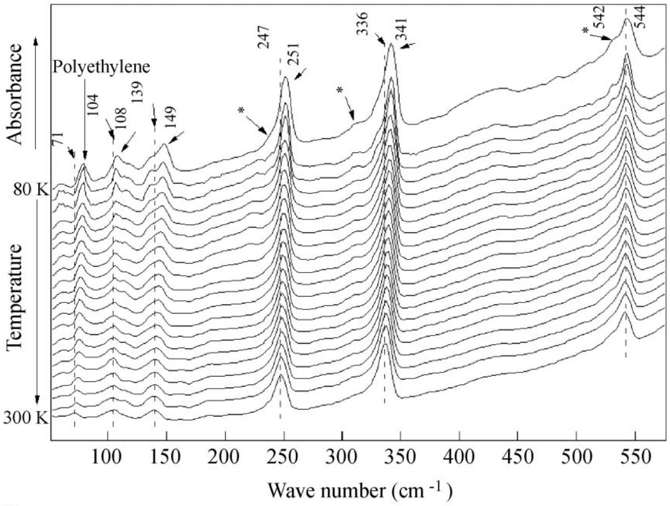

Figure 7
Temperature-dependent series of far-IR absorption spectra of polycrystalline natural-abundance adenine. The temperature range is in 10 K increments from 80 K to 300 K. The spectra for 110 K and 100 K were left out for clarity. The bands indicated by asterisks are poorly resolved in the 300 K spectra, but are clearly present in the 80 K spectra. The data are not corrected for changes in source intensity.

The present study illustrates synchrotron FTIR microspectroscopy experiments to characterize wax deposits formed at the highest depth (or temperature) in oil-producing wells, in an attempt to clarify the physical relationship between the organic material of the deposit and the inorganic phase. The deposits were placed on IR-reflective microscope slides and both IR mapping and random point-and-shoot spectra were collected with 64 scans with 4 cm^{-1} resolution at various deposits, using a 10 × 10 µm aperture size.

Two distinct types of aggregates were found in the spectra presented in Fig. 9: predominantly non-polar (type I) and predominantly polar (type II). However, mixed types or intermediates between the type I and type II were also found within the same aggregate, which clearly demonstrates the advantage of using synchrotron IR spectroscopy in elucidating the physical and chemical bonding of the wax deposits to the inorganic phase.

Type I spectra were characterized by the in-phase rocking for long straight methylene chains at 720 and 730 cm^{-1}, and SH stretching vibrations around 2800 cm^{-1}. FTIR mapping of a single type I aggregate further revealed acidic carbonyl groups that appear to be distributed mainly along the periphery of the aggregate (not shown). This is probably related to the processes associated with oil–water interfacial phenomena and interactions in micro-emulsions. In contrast, type II aggregates contain a higher relative concentration of inorganic material. A comparison of the spectra for $CaCO_3$ and a type-II aggregate (Fig. 10) provides an independent line of evidence about the likely chemical state of trace metals in deepest deposits and is complementary to X-ray fluorescence studies (Chouparova *et al.*, 2002). Furthermore, Si—O stretching vibrations are also present in this type of aggregate. Further study is needed to understand this complex mechanism of aggregate formation that is clearly of interest for chemical and environmental science, and the petroleum industry.

7. Conclusions

As demonstrated by the examples presented in this report, the unique brightness of synchrotron IR light and its high flux in the far-IR

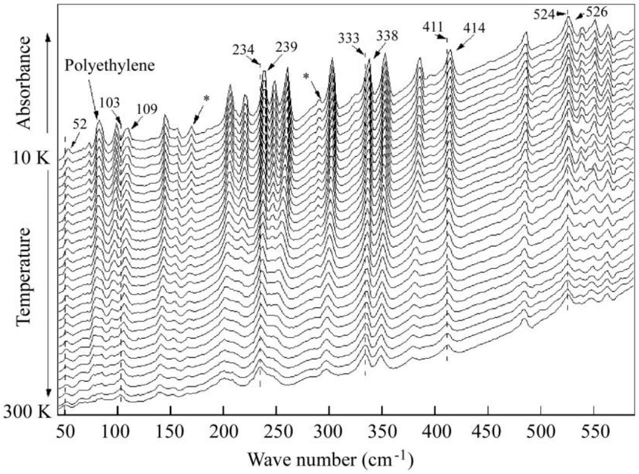

Figure 8
Temperature-dependent series of far-IR absorption spectra of polycrystalline natural-abundance 2-deoxyadenosine. The temperature range is in 10 K increments from 10 to 300 K. The bands indicated by asterisks are poorly resolved in the 300 K spectra, but are clearly present in the 10 K spectra. The data are not corrected for changes in source intensity.

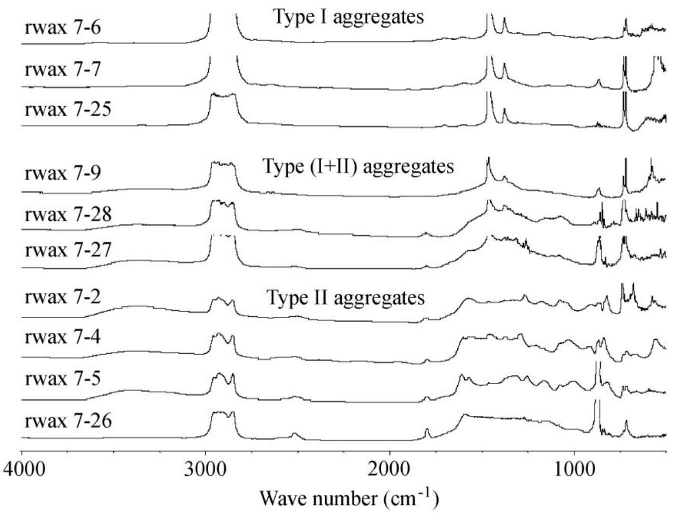

Figure 9
IR spectra of different aggregates observed within a sample of wax deposit extracted from the deepest region of the oil well. Distinctive features are observed in predominantly non-polar aggregates (type I), predominantly polar (type II) and mixed or intermediate aggregates (type I + II).

region make it a valuable tool for the biological sciences. Beamline U2B at the VUV-IR ring of the National Synchrotron Light Source is designed to provide these unique capabilities to the scientific community as well as to continue developing new applications and technologies based on the use of synchrotron IR light.

This work was supported by the NIH Biomedical Technology Program of the Division of Research Resources of NIH (grant P41-RR-01633). The National Synchrotron Light Source at Brookhaven National Laboratory was supported by the Department of Energy, Division of Materials Sciences.

References

Brockwell, D. J., Smith, D. A. & Radford, S. E. (2000). *Curr. Opin. Struct. Biol.* **10**, 16–25.

Bromberg, P. S., Marinkovic, N., Sullivan, M., Toomey, J., Yeh, S.-R., Rousseau, D. L. & Chance, M. R. (2002). *Biophys. J.* **82**, 349*a*.

Camacho, N. P., Rinnerthaler, S., Paschalis, E. P., Mendelsohn, R., Boskey, A. L. & Fratzl, P. (1999). *Bone*, **25**, 287–293.

Carr, G. L. (2001). *Rev. Sci. Instrum.* **72**, 1913–1619.

Carr, G. L., Dumas, P., Hirschmugl, C. J. & Williams, G. P. (1998). *Nuovo Cimento*, D**20**, 375.

Carr, G. L., Reffner, J. A. & Williams, G. P. (1995). *Rev. Sci. Instrum.* **66**, 1490–1492.

Carr, G. L. & Williams, G. P. (1997). *Proc. SPIE*, **3153**, 51–59.

Charriaut-Marlangue, C., Aggoun-Zouaoui, D., Represa, A. & Ben-Ari, Y. (1996). *Trends Neurosci.* **19**, 109–114.

Chouparova, E., Lanzirotti, A., Feng, H., Jones, K. & Marinkovic, N. S. (2002). In preparation.

Duncan, W. D. & Williams, G. P. (1983). *Appl. Opt.* **22**, 2914–2923.

Eaton, W. A., Muñoz, V., Hagen, S. J., Jas, G. S., Lapidus, L. J., Henry, E. R. & Hofrichter, J. (2000). *Annu. Rev. Biophys. Biomol. Struct.* **29**, 327–359.

Haris, P. I. & Chapman, D. (1995). *Biopolymers*, **37**, 251–263.

Huang, R. Y., Miller, L. M., Carlson, C. S. & Chance, M. R. (2002*a*). *Bone*, **30**, 492–497.

Huang, R. Y., Miller, L. M., Carlson, C. S. & Chance, M. R. (2002*b*). Submitted.

Itoh, K., Nakahara, J., Shimanouchi, T., Oya., M., Uno, K. & Iwakura, Y. (1968). *Biopolymers*, **6**, 1759–1766.

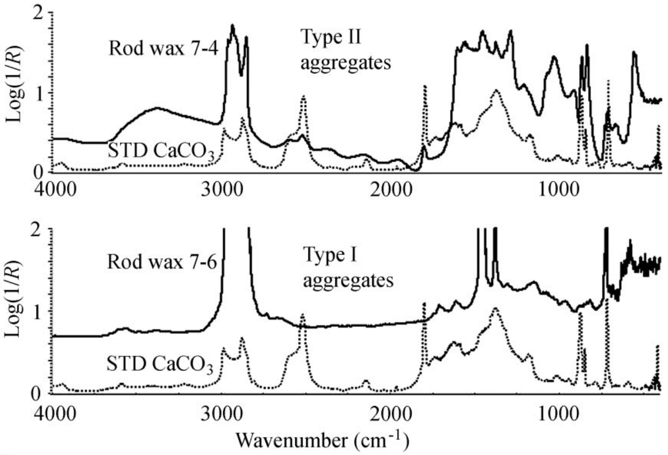

Figure 10
A comparison of spectra for type I and type II aggregates with that of a CaCO$_3$ standard. All carbonate bands appear in polar aggregates.

Jamin, N., Dumas, P., Moncuit, J., Fridman, W. H., Teillaud, J. L., Carr, G. L. & Williams, G. P. (1998*a*). *Proc. Natl Acad. Sci. USA*, **95**, 4837–4840.

Jamin, N., Dumas, P., Moncuit, J., Fridman, W. H., Teillaud, J. L., Carr, G. L. & Williams, G. P. (1998*b*). *Cell Mol. Biol.* **44**, 9–13.

Jerome, C. P., Power, R. A., Obasanjo, I. O., Register, T. C., Guidry, M., Carlson, C. S. & Weaver, D. S. (1997). *Bone*, **20**, 355–364.

Kaufmann, E., Darnton, N. C., Austin, R. H., Batt, C. & Gerwert, K. (2001). *Proc. Natl Acad. Sci. USA*, **98**, 6646–6649.

Koenig, J. L. & Sutton, P. L. (1969). *Biopolymers*, **8**, 167–178.

Lappi, S., Marinkovic, N. S., Franzen, S. & Chance, M. R. (2002). In preparation.

Lira-Galeana, C., Firoozabadi, A. & Prausnitz, J. M. (1996). *Am. Inst. Chem. Eng. J.* **42**, 239–248.

Lira-Galeana, C. & Hammami, A. (2000). *Develop. Petrol. Sci.* B**40**, 557–605.

Marinkovic, N. S., Adzic, A. R., Sullivan, M., Kovacs, K., Miller, L. M., Rousseau, D. L., Yeh, S.-R. & Chance, M. R. (2000). *Rev. Sci. Instrum.* **71**, 4057–4060.

Martin, M. C., Tsvetkova, N. M., Crowe, J. H. & McKinney, W. R. (2001). *Appl. Spectr.* **55**, 111–113.

Melendres, C. A. (1998). *Synchrotron Rad. News*, **3**, 39.

Miller, L. M., Carr, G. L., Jackson, M., Dumas, P. & Williams, G. P. (2000). *Synchrotron Rad. News*, **13**, 31–37.

Miller, L. M., Huang, R. & Chance, M. R. (1999). *Synchrotron Rad. News*, **12**, 21–27.

Miller, L. M., Vairavamurthy, V., Chance, M. R., Mendelsohn, R., Paschalis, E. P., Betts, F. & Boskey, A. L. (2001). *Biochem. Biophys. Acta*, **1527**, 11–19.

Moritsugu, K., Miyashita, O. & Kidera, A. (2000). *Phys. Rev. Lett.* **85**, 3970–3973.

Paschalis, E. P., DiCarlo, E., Betts, F., Sherman, P., Mendelsohn, R. & Boskey, A. L. (1996). *Calcif. Tissue Int.* **59**, 480–487.

Piekut, D., Phipps, B., Pretel, S. & Applegate, C. (1997). *Brain Res.* **743**, 63–69.

Pleshko, N. L., Boskey, A. L. & Mendelsohn, R. (1991). *Biophys. J.* **60**, 786–793.

Reffner, J. A., Martoglio, P. A. & Williams, G. P. (1995). *Rev. Sci. Instrum.* **66**, 1298.

Rey, C., Collins, B., Goehl, T., Dickson, I. R. & Glimcher, M. J. (1989). *Calcif. Tissue Int.* **45**, 157–164.

Rey, C., Shimizu, M. & Glimcher, M. (1990). *Calcif. Tissue Int.* **46**, 384–394.

Rodan, G. A. & Martin, T. J. (2000). *Science*, **289**, 1508–1514.

Sloviter, R. S., Dean, E., Sollas, A. L. & Goodman, J. H. (1996). *J. Comp. Neurol.* **366**, 516–533.

Sperk, G. (1994). *Prog. Neurobiol.* **42**, 1–32.

Sperk, G., Gruber, B., Roder, C. & Schwarzer, C. (1994). *Neuropeptides*, **26**, 44.

Williams, G. P. (1990). *Nucl. Instrum. Methods*, **291**, 8–12.

Xie, A., He, Q., Miller, L., Sclavi, B. & Chance, M. R. (1999). *Biopolymers*, **49**, 591–603.

Xie, A., van der Meer, A. F. G. & Austin, R. H. (2002). *Phys. Rev. Lett.* **88**, 018102-1–01802-4.

Received 18 March 2002 • Accepted 9 May 2002